Optics Letters

Demonstration of multi-plane sharpness metric maximization on motion-compensated, multi-wavelength 3D digital holographic field data

Matthias T. Banet,[1,*] James R. Fienup,[1] and Brian W. Krause[2]

[1] The Institute of Optics, University of Rochester, Rochester, New York 14627, USA
[2] Lockheed Martin Coherent Technologies, 135 S. Taylor Ave., Louisville, Colorado 80027, USA
*matthiasbanet@gmail.com

Received 10 July 2023; revised 17 November 2023; accepted 11 December 2023; posted 11 December 2023; published 14 January 2024

This Letter examines sharpness metric maximization methods on 3D images obtained at Table Mountain, Colorado. We employ multi-wavelength 3D imaging with digital holography and a pilot tone to obtain the aberrated images and use sharpness metric maximization to correct the aberrated images with both pupil-plane and multi-plane corrections. Image quality improves when sharpness metric maximization is used and particularly with multi-plane correction.

https://doi.org/10.1364/OL.499173

Coherent imagery through the atmosphere is degraded by turbulence along the propagation path between the object and the receiver. The strength and distribution of these turbulence aberrations can affect image quality in many different ways. Horizontal-path imaging near the ground features turbulence aberrations that are distributed throughout the propagation path, and the imaging system is considered to be linear, shift variant [1]. In order to correct the image over a finite extent, one requires corrections of the phase of the light in multiple planes between the object and the receiver (or in conjugate locations). Multiconjugate adaptive optics offers one path forward where the phase is physically altered *via* multiple deformable mirrors in order to correct the entire image [2]. This Letter employs a digital solution known as sharpness metric maximization (SMM), where the complex-valued fields are estimated *via* a digital holographic sensor [3,4] and the sharpness [5] of the image is increased by altering the phase digitally at one or more planes within the propagation path [6,7].

SMM for coherent imagery was first introduced by Paxman and Marron [8] for synthetic-aperture radar. Thurman and Fienup [6] demonstrated SMM optically with 2D coherent images produced in the lab and a single corrective phase screen, and Tippie and Fienup [7] repeated the experiment with multiple phase screens along the propagation path. Farriss *et al.* [9] extended the SMM algorithm to accommodate 3D imagery with a single corrective phase screen in simulation, and Banet *et al.* [10] extended these 3D simulated results to include multiple phase screens. This Letter describes taking 3D field data collected at Table Mountain (10 km north of Boulder, CO) and applying SMM to the data in order to obtain corrected imagery. The 3D imaging process is described in detail by Banet and Fienup [11] and is based on a patent developed by Krause [12]. The key difference between the 3D imaging system simulated previously [10] and the one used here is the addition of a second illuminator, called a pilot tone [13], that allows for 3D imaging of moving objects [12] that would otherwise be terribly blurred in the range dimension. SMM experiments for 2D coherent images have similarly taken place at Table Mountain [14].

In the remainder of the Letter, we cover the SMM algorithm that was used for the collected data, describe the experimental setup at Table Mountain and the data processing used to retrieve the digital holograms, and show the corrected 3D imagery.

The SMM algorithm used reverse-mode algorithmic differentiation (RMAD) [15] to calculate the sharpness metric for a given image (the forward model) and the gradients of the sharpness metric with respect to the phase at one or more planes (the gradient model). Our sharpness metric of choice was given by

$$S = S_1 + \alpha \Psi_q, \tag{1}$$

where S_1 is the base sharpness term given by

$$S_1 = \operatorname{sgn}(\beta - 1) \sum_{x,y} I_n^{\beta}(x, y), \tag{2}$$

where $I_n(x, y)$ is the 2D frequency-averaged irradiance image of the object for the n^{th} time segment with transverse coordinates (x, y), and β is the sharpness exponent [5]. The variable Ψ_q is a quadratic-phase regularizer that attempts to prevent demagnification [7] from occurring in the sharpened images and is given by Eq. (13) in Ref. [10]. The coefficient, α, multiplying Ψ_q allows us to vary the strength of that term relative to S_1. The SMM algorithm was modified to accommodate the fact that the total image collection occurred over 80 ms, which is long enough for the turbulence to evolve significantly. Hence, we divided the image collection into 8 segments (each 10 ms long) and independently performed 2D SMM on the average 2D irradiance image, $I_n(x, y)$, for each segment. This allowed us to obtain estimates of the turbulence phase as the atmosphere evolved.

In Ref. [10], the 3D irradiance image, given by $I(x, y; z)$, where z is the range coordinate, was formed by Fourier transforming a stack of complex-valued images over the optical frequency

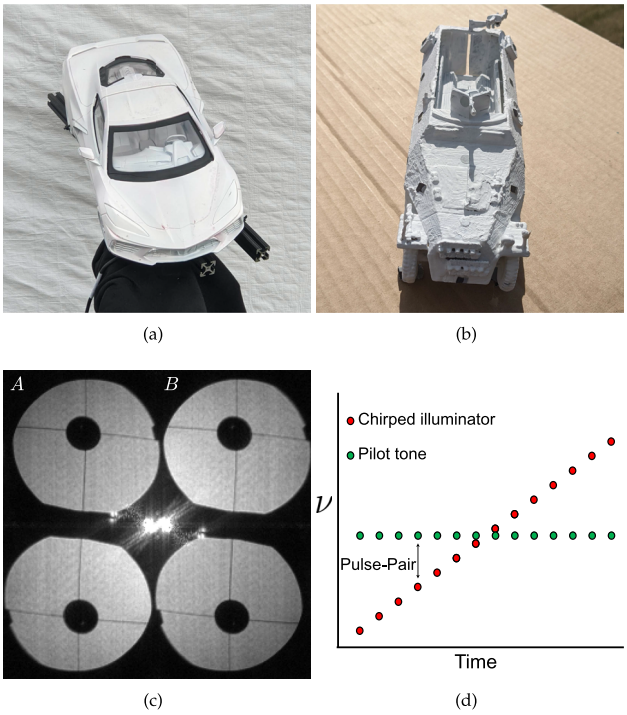

Fig. 1. (a) White-painted toy sports car, (b) white-painted toy half-track, (c) example Fourier plane showing A, the pilot-tone pupil and B, the chirped illuminator pupil, and (d) diagram depicting the two pulse-trains used.

dimension and taking the squared modulus of the result. Here, with the addition of the pilot tone, we generated 2 stacks of complex-valued images (one stack for each illuminator), multiplied one stack by the complex conjugate of the other, and then Fourier transformed that result over frequency and took the squared modulus to obtain $I(x, y; z)$. Here, 2D SMM was applied to each time segment, and the corrective phase estimates for each time segment were applied to images from both illuminators to generate motion-compensated 3D images. The 3D images utilized 2D images collected over the entire 80 ms.

We used $\beta = 0.5$, as this offered the best-looking corrected images after testing the data with a range of β values (from 0.01 to 1.1). Additionally, $\beta = 0.5$ corresponds to an optimal value when provided frames with few independent speckle realizations [16], which was relevant for some features in the images (i.e., the stationary background).

We collected digital holographic field data of two different objects at Table Mountain. The first object, shown in Fig. 1(a), was a white-painted toy sports car, which was imaged on September 2, 2021, and the second, in Fig. 1(b), was a white-painted toy half-track with unresolved retro-reflective stickers scattered over the object, which was imaged on June 29, 2022. We illuminated the object with two simultaneous pulse trains, shown in Fig. 1(d). For the chirped illuminator, the pulse train's temporal frequency varied linearly in time, and for the pilot tone, the temporal frequency was constant in time. The central wavelength of each illuminator was $\lambda_0 = 1.535\ \mu$m (corresponding to a frequency of $\nu_0 = 195.3$ THz), and the chirped illuminator had a frequency range, or optical bandwidth, $\Delta\nu$, that was in the 10's of GHz. The light for each illuminator propagated through a common transmitter fiber and passed through beam divergence optics before propagating to the object located a distance of $z_0 = 400$ m away. During each image collection time, we rotated the object on a rotation stage to achieve significant speckle noise reduction in the final images.

Light scattered from the object and propagated to a 30 cm aperture near the illumination optics. We collected the light, in the common aperture, from each pulse pair within the pulse train. We interfered each signal return with its respective reference beam in the off-axis image-plane recording geometry [4]. The reference beams each exited a fiber in a conjugate pupil plane. For a given pulse pair, we spatially multiplexed the interference patterns associated with each pulse onto the same hologram [17], and, after performing a 2D Fourier transform, gained access to the complex-valued pupil fields in the Fourier plane. The off-axis positioning of each fiber allowed for separation of the desired signal terms in the Fourier plane. Figure 1(c) shows an example Fourier plane with the desired pupil terms A, corresponding to the pilot tone, and B, corresponding to the chirped illuminator.

Before windowing either of the pupil terms, we applied hologram correction terms that would correct for any small focusing errors in the Fourier plane that resulted from mis-positioning of the reference beam fibers in the z direction. These hologram correction terms were obtained by optimizing the sharpness of the pupils in the Fourier plane with a corrective defocus term in the hologram plane. A different hologram correction term was applied for each pupil, A and B, within a pulse pair, and each was windowed separately within the Fourier plane. Once the pupils were sharpened and windowed, we applied an isoplanatic pupil correction term to correct for static system aberrations. The pupil correction term was determined by performing SMM on the imagery with a corrective phase term in the pupil plane comprised of Zernike polynomials. The images used in this optimization process were collected over time scales which allowed the atmospheric turbulence to evolve greatly, which meant the effects of turbulence were averaged out and the optimization provided estimates of the static aberrations due to the system alone. The steps laid out here were applied to each pulse pair within the duration of the pulse train, or "ramp". In these experiments, there were always 200 pulse pairs in a ramp.

Once the two stacks of pupil frames were obtained, we propagated each pupil frame digitally to an object plane, resulting in the two stacks of complex-valued images referred to previously. Next, we took the conjugate-product of the image stacks and Fourier transformed the result over frequency to obtain a complex-valued 3D image and the 3D irradiance, $I(x, y; z)$. Because visualizing 3D images is troublesome on 2D displays, we instead present two types of 2D images that are more instructive: The first is a 2D projected irradiance image that simply projects the 3D irradiance, $I(x, y; z)$, along the z dimension. The second is a range image which is determined by taking the z-location of maximum irradiance for every (x, y) pixel to be the range at that pixel. For more information on range image formation, we refer the reader to Ref. [11]. These two types of 2D images will be examined for each of the two objects.

It should be noted that, initially, the 3D images had severe blur in the z direction due to global piston phase errors for the pulse pairs. These errors were random from pulse-to-pulse, and, in order to compensate for this, we used phase-gradient autofocus applied to 3D data [18] to determine an estimate of the global piston phase errors.

We fed the complex-valued pupil data from both illuminators to the SMM algorithm [10], which involved digitally placing

corrective phase screens at one or more locations along the propagation path and iteratively calculating sharpness and the gradient of sharpness with respect to the phase screens for each iteration. Our optimizer of choice was the limited-memory Broyden Fletcher Goldfarb Shanno (L-BFGS) algorithm [19]. We performed both isoplanatic SMM (with a single corrective phase screen in the pupil) and multi-plane SMM, with 10 corrective phase screens positioned *via* the method developed by Paxman *et al.* [20], for each object in question.

We employed a Scintec BLS900 scintillometer during our image collections that estimated the average index-of-refraction structure parameter, C_n^2, over a propagation path nearby the path used to the image the objects. For the first image—the September 2, 2021 collection—the scintillometer measurement nearest in time to the image collection was $C_n^2 = 2.4 \times 10^{-14}\ \mathrm{m}^{-2/3}$ which yields $D/r_0 = 2.1$ and an isoplanatic angle of $\theta_0 = 110\ \mu\mathrm{rad}$, and for the second image—the June 29, 2022 collection—the scintillometer measurement nearest in time was $C_n^2 = 7.0 \times 10^{-14}\ \mathrm{m}^{-2/3}$ which yields $D/r_0 = 4.0$ and $\theta_0 = 59\ \mu\mathrm{rad}$. The calculations assume uniform turbulence strength over the propagation path, which is a reasonable assumption given the flat, mesa-like terrain of Table Mountain. The scintillometer propagation path deviated from the image collection propagation path by about 15°. Furthermore, the instantaneous C_n^2 in the atmosphere can vary as a function of location and even over the course of an image collection. Hence, the calculations above should be taken as rough estimates.

The imaging parameters for the two images were as follows. Both images had the same diffraction-limited transverse resolution given by $\rho = \lambda_0 z_0/D = 2.0\,\mathrm{mm}$. The first image employed a bandwidth of $\Delta\nu = 38\,\mathrm{GHz}$, which yielded a range resolution of $\delta_z = c/(2\Delta\nu) = 3.9\,\mathrm{mm}$, and the second image employed a bandwidth of $\Delta\nu = 34\,\mathrm{GHz}$, which yielded a range resolution of 4.4 mm. For the first image, the camera recorded 200 multiplexed holograms (one for each pulse pair) at 2.5 kHz with image sizes of 448×448 pixels. The image plane sampling quotient [4] was around 2.1. After windowing the pupils, we padded them by a factor of 2 which brought the final image size to 424×424 pixels with a 1D field of view of 44 cm. For the second image, the camera recorded 200 multiplexed holograms at 2.5 kHz with image sizes of 256×256 pixels. The image plane sampling quotient [4] was around 2.1. After windowing the pupils, we padded them by a factor slightly greater than 2 to bring the final image size to 256×256 pixels with a 1D field of view of 25 cm.

For the first image, the isoplanatic patch size corresponding to the isoplanatic angle, θ_0, was $z_0\theta_0 = 4.5\,\mathrm{cm}$, and, for the second image, the isoplanatic patch size was 2.4 cm. For both imaging scenarios, the isoplanatic patch size was many (10-20) transverse resolution elements in extent, but for each scenario there were about 10 isoplanatic patches across the entire field of view (although fewer across the objects of interest within the field of view). This presents a scenario where one would desire multi-plane correction *via* SMM to sharpen the entire image extent, even though the D/r_0 values for each image are relatively weak.

For the first image collection, of the toy car, we fed the pupil data to the SMM algorithm and optimized the 10 corrective phase screens in order to the maximize the sharpness metric in Eq. (1). We used the method of sieves (which is a form of bootstrapping) as described in Ref. [10] and assumed uniform turbulence over the propagation path. We began optimizing with Gaussian kernel standard deviations of 16 cm and decreased the kernel size by a factor of 2 for each round of sequential optimization ending in a kernel size of 0.5 cm. We always performed a round of point-by-point optimization afterwards, totaling 7 rounds of optimization, where each consisted of 5 L-BFGS iterations. For the first image collection we used $\alpha = 0$, which corresponded to no quadratic phase regularization, as little demagnification occurred.

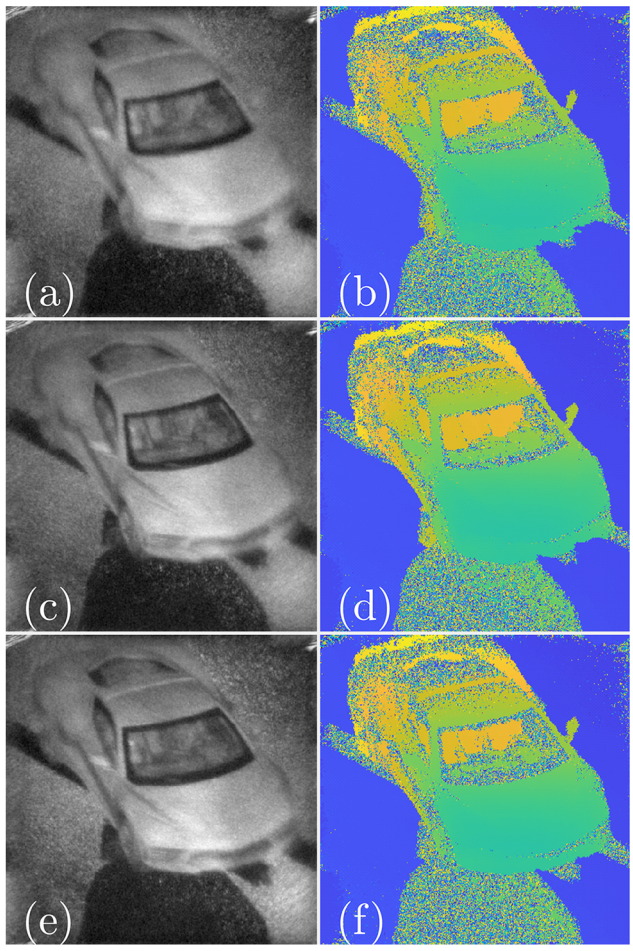

Fig. 2. The original aberrated (a) projected irradiance and (b) range images, the pupil-plane corrected (c) projected irradiance and (d) range images, and the multi-plane corrected (e) projected irradiance and (f) range images of the toy sports car.

Figure 2 shows projected irradiance images (left column) and range images (right column) for the original aberrated image (top row), pupil-plane corrected image using a single corrective phase screen (middle row), and multi-plane corrected image using 10 corrective phase screens. The image quality in both columns increases going from the uncorrected, to the single correction plane, and to the multiple planes of correction. Due to the weak turbulence here, the differences are slight, but still noticeable. Comparing Fig. 2(a) to Fig. 2(c), the overall blur is less after pupil-plane correction. Comparing Fig. 2(c) to Fig. 2(e), certain areas of the image are sharper after multi-plane correction. For example, the black border around the windshield is appropriately darker and the crease on the roof of the car appears sharper in Fig. 2(e). Additionally, the dark support strut directly underneath (in front of) the car is noticeably sharper in the multi-plane image. In Fig. 2(f), there is more range noise coincident with the black border around the windshield, particularly at the

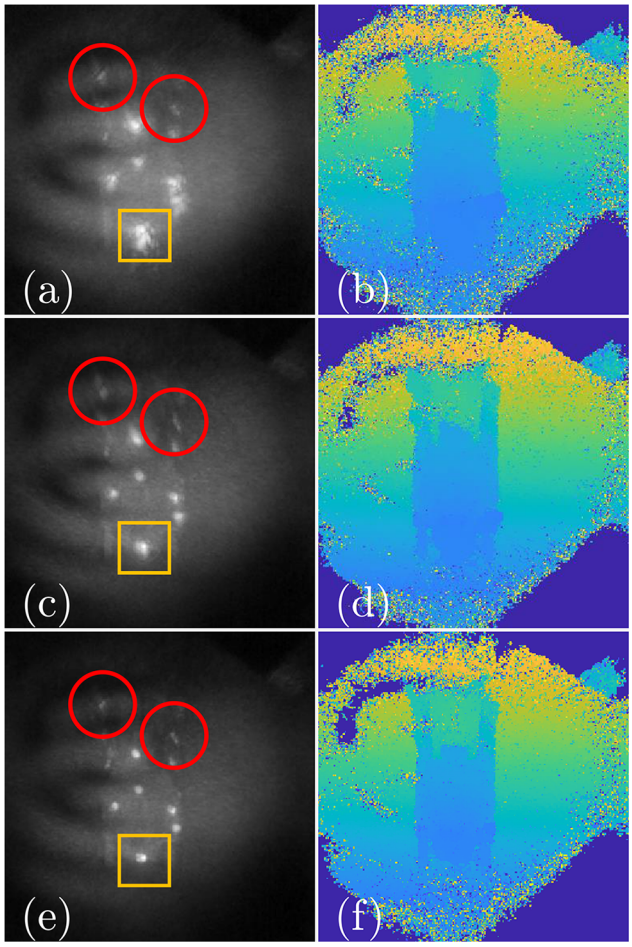

Fig. 3. The original aberrated (a) projected irradiance and (b) range images, the pupil-plane corrected (c) projected irradiance and (d) range images, and the multi-plane corrected (e) projected irradiance and (f) range images of the toy half-track.

top and sides of the windshield, which is fundamentally due to multi-plane SMM sharpening the edges which results in less light from nearby bright pixels from entering the black border. This results in lower signal return within the black border and thus noisier range reports, which is actually indicative of the true, underlying object reflectance and, thus, is a more desirable result.

For the second image collection, of the toy half track, the SMM algorithmic procedure was identical to the one for the first image, except we set $\alpha = 10^3$ for the multi-plane case in order to prevent demagnification. In Fig. 3, we show results in a similar fashion to Fig. 2. Again, image quality for both columns increases progressively row-to-row. The jump in quality between the pupil-plane corrected and multi-plane corrected images is more noticeable here due to (1) the stronger turbulence and (2) the retro-reflectors that make the anisoplanatism more apparent. The blur functions differ for the retro-reflectors in Fig. 3(a), and the pupil-plane correction fails to sharpen them all in Fig. 3(c). In fact, some retro-reflectors actually look blurrier in the pupil-plane corrected case, Fig. 3(c), when compared to the original aberrated case, Fig. 3(a), which is indicative of anisoplanatism (as is seen in the red circled regions). Additionally, the bottom-most retroreflector (orange box) is clearly the sharpest in the multi-plane corrected case. In the range images, the left and right edges of the half-track become sharper, the range chatter lessens, and the dim regions become more noticeable in each progressive row in Fig. 3. Note how Fig. 3 is an example of a case where the range images offer a great deal more information than the irradiance images. For example, the non-uniform illumination and retro-reflectors somewhat obscure the underlying object reflectance, but the fine features of the object are more recognizable in the range channel (e.g., the turret and front tires).

This study demonstrates motioned-compensated, multi-wavelength 3D imaging on field data and uses SMM to sharpen the images. The first image set demonstrates multi-plane SMM in the field with an uncooperative moving object and the second image set demonstrates multi-plane SMM with a moving object enhanced with retro-reflectors to emphasize the anisoplanatic correction. The results show that both the projected irradiance images and the range images improve in quality after SMM and moreso when a multi-plane approach is used.

Funding. Air Force Research Laboratory (FA8649-20-C-0318).

Disclosures. The authors declare that there are no conflicts of interest related to this article.

Data availability. Data underlying the results presented in this paper are not publicly available at this time but may be obtained from the authors upon reasonable request.

REFERENCES

1. D. Korff, G. Dryden, and R. Leavitt, J. Opt. Soc. Am. **65**, 1321 (1975).
2. D. C. Johnston and B. M. Welsh, J. Opt. Soc. Am. A **11**, 394 (1994).
3. J. W. Goodman and R. Lawrence, Appl. Phys. Lett. **11**, 77 (1967).
4. M. F. Spencer, R. A. Raynor, M. T. Banet, and D. K. Marker, Opt. Eng. **56**, 031213 (2016).
5. J. R. Fienup and J. J. Miller, J. Opt. Soc. Am. A **20**, 609 (2003).
6. S. T. Thurman and J. R. Fienup, J. Opt. Soc. Am. A **25**, 995 (2008).
7. A. E. Tippie and J. R. Fienup, Opt. Lett. **35**, 3291 (2010).
8. R. G. Paxman and J. C. Marron, Proc. SPIE **0976**, 37 (1988).
9. W. E. Farriss, J. R. Fienup, J. W. Stafford, and N. J. Miller, Proc. SPIE **10772**, 107720K (2018).
10. M. T. Banet, J. R. Fienup, J. D. Schmidt, and M. F. Spencer, Appl. Opt. **60**, G243 (2021).
11. M. T. Banet and J. R. Fienup, Opt. Eng. **62**, 073103 (2023).
12. B. W. Krause, "Motion compensated multi-wavelength digital holography," U.S. patent 9,581,967 (28Feb2017).
13. B. W. Krause, B. G. Tiemann, and P. Gatt, Appl. Opt. **51**, 8745 (2012).
14. J. C. Marron, R. L. Kendrick, N. Seldomridge, T. D. Grow, and T. A. Höft, Opt. Express **17**, 11638 (2009).
15. A. S. Jurling and J. R. Fienup, J. Opt. Soc. Am. A **31**, 1348 (2014).
16. S. T. Thurman and J. R. Fienup, J. Opt. Soc. Am. A **25**, 983 (2008).
17. S. T. Thurman and A. Bratcher, Appl. Opt. **54**, 559 (2015).
18. J. W. Stafford, B. D. Duncan, and D. J. Rabb, Appl. Opt. **55**, 4611 (2016).
19. S. Wright and J. Nocedal, Springer Science **35**, 7 (1999).
20. R. G. Paxman, B. J. Thelen, and J. J. Miller, Proc. SPIE **3763**, 2 (1999).